UC Berkeley

Title

Isotopic insights into methane production, oxidation, and emissions in Arctic polygon tundra

Authors

Vaughn, Lydia JS
Conrad, Mark E
Bill, Markus
et al.

Isotopic insights into methane production, oxidation, and emissions in Arctic polygon tundra

Lydia J. S. Vaughn, Mark E. Conrad, Markus Bill, Margaret S. Torn

Abstract

Arctic wetlands are currently net sources of atmospheric CH_4. Due to their complex biogeochemical controls and high spatial and temporal variability, current net CH_4 emissions and gross CH_4 processes have been difficult to quantify, and their predicted responses to climate change remain uncertain. We investigated CH_4 production, oxidation, and surface emissions in Arctic polygon tundra, across a wet-to-dry permafrost degradation gradient from low-centered (intact) to flat- and high-centered (degraded) polygons. From 3 microtopographic positions (polygon centers, rims, and troughs) along the permafrost degradation gradient, we measured surface CH_4 and CO_2 fluxes, concentrations and stable isotope compositions of CH_4 and DIC at three depths in the soil, and soil moisture and temperature. More degraded sites had lower CH_4 emissions, a different primary methanogenic pathway, and greater CH_4 oxidation than did intact permafrost sites, to a greater degree than soil moisture or temperature could explain. Surface CH_4 flux decreased from 64 nmol m^{-2} s^{-1} in intact polygons to 7 nmol m^{-2} s^{-1} in degraded polygons, and stable isotope signatures of CH_4 and DIC showed that acetate cleavage dominated CH_4 production in low-centered polygons, while CO_2 reduction was the primary pathway in degraded polygons. We see evidence that differences in water flow and vegetation between intact and degraded polygons contributed to these observations. In contrast to many previous studies, these findings document a mechanism whereby permafrost degradation can lead to local decreases in tundra CH_4 emissions.

Introduction

The high-latitude permafrost region plays an important role in the global carbon budget. Historically, this region's soils have been a large net source of atmospheric CH_4, and future CH_4 emissions under climate change remain uncertain. (McGuire et al., 2009, 2012; Mastepanov et al., 2013). Arctic CH_4 emissions are difficult to accurately measure, model, and predict, as complex controls on CH_4 processes generate highly variable CH_4 emissions in both space and time (Whalen & Reeburgh, 1992; Bridgham et al., 2013; Olefeldt et al., 2013). Current estimates of high-latitude CH_4 emissions range widely from 9 to 35 Tg CH_4 yr^{-1} (McGuire et al., 2012), and while most models predict emissions will increase with climate change and associated permafrost degradation (Koven et al., 2011; Schuur et al., 2013; Lawrence et al., 2015), the magnitude and geographic distribution of this change depend on numerous ecological variables such as soil moisture, water table position, thaw depth, temperature, microbial community, and vegetation composition, stature, and productivity (Wagner et al., 2003; Von Fischer et al., 2010; Sturtevant et al., 2012; Tagesson et al., 2012; Mastepanov et al., 2013; Olefeldt et al., 2013). Together, these variables control a suite of processes determining net CH_4 emissions: CH_4 production by methanogenic archaea, CH_4 oxidation by methanotrophic bacteria, and CH_4 transport to the atmosphere (Chanton, 2005; Chanton et al., 2005).

A number of field studies have assessed CH_4 emissions across stages of permafrost degradation, finding that thaw-induced subsidence can increase CH_4 emissions and alter methanogenic pathways (Wickland *et al*., 2006; Olefeldt *et al*., 2013; Hodgkins *et al*., 2014; Johnston *et al*., 2014; McCalley *et al*., 2014), with strong correlations between net CH_4 emissions and specific microbial processes (Mondav *et al*., 2014). These studies underscore the importance of gross metabolic processes as controls on net CH_4 flux and the responsiveness or sensitivity of these processes to thaw-induced changes. Critically, in all of these studies, permafrost thaw increased inundation and active layer thickness due to thermokarst subsidence. In many landscapes, however, permafrost thaw can reduce inundation, as loss of subsurface ice creates drainage channels, redistributing water away from wetlands (Fortier *et al*., 2007; Godin *et al*., 2014). Such soil drying and reductions in high-latitude wetland area are predicted to be key controls on future Arctic CH_4 emissions (Riordan *et al*., 2006; Bohn *et al*., 2007; Avis *et al*., 2011; Koven *et al*., 2011), but few field studies have measured CH_4 emissions and their biogeochemical controls along wet-to-dry gradients of permafrost degradation.

Using a wet-to-dry permafrost degradation gradient, this study evaluates gross CH_4 processes and net CH_4 emissions across stages of drainage and geomorphic succession. In ice-wedge polygon tundra in Barrow, Alaska, we combine stable isotope depth profiles with surface flux measurements to investigate process-level controls on surface CH_4 emissions. We ask (1) how do CH_4 production and consumption processes vary across geomorphic and temporal gradients, and (2) how do these subsurface CH_4 processes relate to surface greenhouse gas fluxes? This study makes use of two geomorphic gradients and one temporal gradient: an ice-wedge thaw gradient spanning low-centered to flat-centered and high-centered polygons, a finer scale gradient of individual polygon features (centers, rims, and troughs), and a seasonal gradient from July–October.

Covering ~250 000 km² throughout the Arctic (Donner *et al*., 2007), polygon tundra is characterized by ice-wedge polygons, microtopographic features ~10–30 m in diameter that are separated by lower-lying, often wet or inundated channels called troughs. These polygons may be classified as low-centered polygons, which have low, wet centers bordered by raised, relatively dry rims; high-centered polygons, with high, well-drained centers and no clear rim delineation; or flat-centered polygons, with intermediate relief between high-centered and low-centered polygons. Polygons form from the growth and thaw of subsurface ice formations known as ice wedges. During earlier polygon successional stages, ice wedges underlie the troughs of low-centered polygons (Brown, 1967), impeding drainage and causing soil uplift through their annual growth and expansion (Drew & Tedrow, 1962). If these primary ice wedges thaw, erosion of polygon rims can drain the centers of low-centered polygons, leading to the growth of secondary ice wedges and formation of high-centered polygons (Drew & Tedrow, 1962; Billings & Peterson, 1980; MacKay, 2000; Huryn & Hobbie, 2012; Ping *et al*., 2015). This form of permafrost degradation produces drier equilibrium landscapes, which in the near term are not necessarily accompanied by increased active layer thickness. Between low-centered and high-centered polygons, differences in drainage and subsurface ice properties create strong thermal, hydrological, and geochemical gradients (Liljedahl *et al*., 2012; Hubbard *et al*., 2013; Newman *et al*., 2015; Wainwright *et al*., 2015).

Succession from low-centered to high-centered polygons has accelerated in Alaska, where thermokarst development over the past three decades has greatly outpaced the historical background landscape succession

rate (Jorgenson *et al*., [2006](#)). Such changes in soil moisture and inundation have large implications for CH_4 emissions. Previous research in polygon-dominated landscapes has found lower CH_4 emissions with decreased soil moisture (Rhew *et al*., [2007](#); Von Fischer & Hedin, [2007](#); Von Fischer *et al*., [2010](#)), less inundated area (Sturtevant *et al*., [2012](#)), and lower water table position (Kutzbach *et al*., [2004](#)). A more limited set of studies evaluating CH_4 emissions has treated polygon types as distinct geomorphic units, finding higher CH_4 fluxes from low-centered than high-centered polygons (Sachs *et al*., [2010](#); Wainwright *et al*., [2015](#)). No studies to our knowledge, however, have related net CH_4 emissions to gross metabolic CH_4 processes across a range of polygon features.

To investigate CH_4 production, oxidation, and net emissions, this study combines surface trace gas flux measurements with concentrations and stable isotope measurements of CH_4 and co-occurring CO_2. While net CH_4 fluxes are straightforward to measure, the component processes of CH_4 production and oxidation (hereafter referred to as gross processes) cannot be directly observed *in situ* without an added tracer or inhibitor (Frenzel & Bosse, [1996](#); Von Fischer & Hedin, [2007](#)). The stable isotope compositions of CH_4 provide an indirect approach, as these gross processes fractionate carbon and hydrogen isotopes in characteristic ways. Isotope discrimination during methanogenesis produces CH_4 that is highly depleted in ^{13}C and ^{2}H, whereas CH_4 oxidation enriches the residual CH_4 in the heavier isotopes (Whiticar *et al*., [1986](#); Chanton *et al*., [2005](#); Hornibrook & Aravena, [2010](#)). Stable isotope analyses have been used to assess CH_4 production pathways (Hornibrook *et al*., [1997](#); Conrad, [2005](#)), fractional and absolute CH_4 production and oxidation rates (Liptay *et al*., [1998](#); Chanton & Liptay, [2000](#)), CH_4:CO_2 production ratios (Corbett *et al*., [2013](#), [2015](#)), and CH_4 transport through hollow plant tissues (Chanton, [2005](#); Hornibrook, [2009](#)).

Future high-latitude CH_4 emissions will depend largely on changes in wetland area (Bohn *et al*., [2007](#); Avis *et al*., [2011](#); Koven *et al*., [2011](#)). Field studies are needed to evaluate CH_4 emissions as landscapes become drier or wetter due to thaw, subsidence, and drainage. This study integrates measurements of net CH_4 fluxes and gross CH_4 production and oxidation along a wet-to-dry permafrost degradation gradient in Arctic polygon tundra. Together, this information can be used to identify mechanistic changes underlying net emissions outcomes and identify critical positions in the landscape such as particular polygon features that may disproportionately influence the response of landscape-scale CH_4 fluxes to permafrost degradation.

Materials and methods

Site

The Barrow Environmental Observatory (BEO) is located ~6 km east of Barrow, AK (71.3°N, 156.5°W). At the northern tip of Alaska's Arctic coastal plain, Barrow has a maritime climate characterized by long, dry winters and short, moist, cool summers, with a mean annual air temperature of −12 °C and mean annual precipitation of 106 mm. Continuous ice-rich permafrost extends to >400 m (Hinkel & Nelson, [2003](#)), overlain by a shallow active layer whose depth varies spatially and interannually from approximately 20 to 60 cm. In and around the BEO, a region of interstitial tundra among thaw lakes and drained thaw lake basins, the land surface has low topographic relief reaching a maximum elevation of ~5 m (Brown *et al*., [1980](#); Hubbard *et al*., [2013](#)), with ~65%

of the ground surface organized into ice-wedge polygons (Brown *et al*., [1980](); Lara *et al*., [2014]()). Soils in the region are primarily Typic Aquiturbels (53%), Typic Histoturbels (22%), and Typic Aquorthels (8.6%) (Bockheim *et al*., [1999]()), formed from late Pleistocene-aged sediments of the Gubik Formation (Black, [1964]()), with low sulfate and nitrate concentrations and abundant iron (Herndon *et al*., [2015a](); Newman *et al*., [2015]()). Vegetation cover, height and dominant species vary between polygon types and microtopographic features (Billings & Peterson, [1980](); Minke *et al*., [2009]()). The most abundant vascular plant species include the wet tundra graminoids *Carex aquatilis*, *Eriophorum* species, and *Dupontia fisheri*. Mosses and lichens cover much of the land surface as well, along with limited shrub, forb, and dry tundra graminoid species (Brown *et al*., [1980](); Villarreal *et al*., [2012]()).

Field measurements and sample collection

For sample collection and field measurements, we selected seven ice-wedge polygons covering a gradient of microtopographic features and subsurface ice properties. We divided these polygons into two categories: (1) low-centered polygons (LC polygons, *n* = 3), with inundated, low-lying centers, large, intact ice wedges, and ice-rich permafrost; and (2) flat/high-centered polygons (FHC polygons, *n* = 4), with flat- to high-center relief, smaller, more degraded ice wedges, and lower permafrost ice contents (Hubbard *et al*., [2013]()). Within each polygon, we established three 1 × 1 m plots, in the polygon's center, rim, and trough, totaling 21 plots. If a FHC polygon lacked a clearly raised rim, we placed the rim plot at the upper limit of the slope between the raised center and the trough. This sampling scheme was thus organized at three levels of spatial resolution: two polygon types (LC polygon and FHC polygon); three polygon positions (center, rim, and trough); and six polygon features, defined as type × position (center, rim, and trough of each polygon type).

From each of these plots, we measured CH_4 flux and ecosystem respiration (R_{eco}), soil moisture, soil temperature, and concentrations and $\delta^{13}C$ of soil pore space CH_4 and CO_2. We measured fluxes of CO_2 and CH_4 on July 10–12, August 7–16, September 4–7, and October 2–4, 2013, using opaque static chambers (25 cm diameter, 15–20 cm height). Chambers were tall enough to enclose vegetation and were vented according to Xu *et al*. ([2006]()) to minimize pressure excursions due to the Venturi effect. In inundated plots, we used a floating chamber whose base extended 4 cm below the water surface. In all other plots, chambers were seated on PVC bases extending ~15 cm below the soil surface. To minimize disturbance, we installed these bases in June 2013 and left them in place throughout the sampling season. For each flux measurement, we seated the chamber in a 3-cm-deep, water-filled trench in the base's top rim to create an airtight seal. Using a Los Gatos Research, Inc. (LGR) portable Greenhouse Gas Analyzer, we recorded CO_2 and CH_4 concentrations within the chamber over 4–8 min and calculated the flux rate of each gas from the slope of the linear portion of the concentration vs. time curve. As chambers were opaque with no light penetration, measured CO_2 fluxes were equivalent to R_{eco}. Soil moisture and soil temperature were recorded concurrently with each greenhouse gas flux measurement. We measured volumetric water content in the top 10 cm of soil or standing water with a MiniTrase time domain reflectometer (Soilmoisture Equipment Corp.) and soil temperature at 10 cm depth with a thermistor probe. As vegetation and inundation status varied between plots, depths of moisture and temperature measurements were determined from the top of the moss layer, bare soil, or water surface.

On August 7–11, 2012, July 12–14, 2013, August 10–16, 2013, September 3–8, 2013, and October 2–5, 2013, we collected soil pore water or gas from depths of 10 cm, 20 cm, and the full depth of the thawed layer, approximately 2 cm above the frozen layer. When thaw depth was 20 cm or less, we collected samples from only two depths. Samples were collected using ¼″ diameter stainless steel probes inserted in the plots during August 2012 and June 2013, sealed with airtight caps, and left in place throughout the sampling season to reduce disturbance from repeated insertion and removal. At each sampling time, we removed the cap, connected ¼″ inner diameter tubing to the probe, and used a peristaltic pump to draw subsurface water or gas through the tubing into a 60-mL syringe. To minimize sample contamination, we assessed tubing and connections for leaks and fully purged the system with soil gas or water before attaching a sampling syringe. If the sampling probe became clogged by thick vegetation or wet soil, we removed the probe, cleaned it, and re-inserted it ~10 cm from the previous insertion point. We filtered water samples in the field through 0.1 μm syringe filters and injected them directly into evacuated glass vials sealed with 14 mm-thick chlorobutyl septa (Bellco Glass, Inc., Vineland, NJ, USA). In cases where syringes contained a mixture of water and gas, we collected and analyzed both sample types. When transferring samples from syringes to vials, precautions were taken to prevent any loss of headspace gas; samples were isolated from the atmosphere using syringe stopcocks and in-line syringe filters, and needles were slowly removed from vials after injection to allow septa to properly to reseal. Samples were stored at 4 °C for up to 1 month in Barrow and then transported to Berkeley, CA, for analysis. Vials and septa were tested for loss or exchange of headspace gas over this period.

Laboratory analyses and isotope calculations

All isotope and concentration analyses were conducted at the Center for Isotope Geochemistry (CIG) at Lawrence Berkeley National Laboratory, Berkeley, CA. We measured carbon isotope ratios of dissolved inorganic carbon (DIC) in water samples and CO_2 in gas samples using a variation on the technique outlined in Torn *et al*. (2003). We report carbon isotope ratios in parts per thousand (‰) using the conventional δ-notation relative to Vienna Peedee Belemnite (VPDB), where $\delta^{13}C = (R_{sample}/R_{standard} − 1) \times 1000$ and R is the abundance ratio of the light to heavy isotope. The carbon isotope ratios of DIC or CO_2 are accurate to ±0.33‰ (1σ) based upon repeated analyses of the laboratory standards.

Carbon isotope ratios of higher concentration CH_4 samples (>300 ppmv) were measured using a trace gas ultra system interfaced to a Delta V Plus mass spectrometer (Thermo Fisher Scientific, Bremen, Germany). CH_4 was chromatographically separated from other gases in the trace gas ultra system using an HP-molesieve fused-silica capillary column (30 m × 0.320 mm). The CH_4 was then combusted to CO_2 at 1000 °C in a capillary ceramic tube loaded with Ni, Cu, and Pt wires, dried, and transferred to the IRMS for the carbon isotope measurements. The reproducibility of measured CH_4 $\delta^{13}C$ values using this method is estimated to be ± 0.16‰ (1σ) based on repeated analyses of an in-house laboratory standard. The $\delta^{13}C$ values of lower concentration CH_4 samples were analyzed using the trace gas preconcentration system interfaced with a Micromass mass spectrometer as described in Torn *et al*. (2003). Up to 60 mL of gas was injected into the trace gas where CO_2 and water vapor were chemically stripped from the gas before combusting the CH_4 at 1000 °C and cryogenically preconcentrating the resulting CO_2 prior to analysis in the mass spectrometer. The reproducibility of these analyses is ±0.3‰ (1σ). $\delta^{13}C$ measurements of CH_4, DIC, and CO_2 were corrected for 3–5‰ systematic

offsets between the measured δ¹³C values of in-house standards and their known isotopic compositions, calibrated with external standards.

Concentrations of CH_4 and CO_2 in gas samples were determined using a 2014 Shimadzu GC. Approximately 4.5 mL of gas headspace from sample vials was flushed through a 1 mL stainless steel loop. The two gases were then isolated on a HayeSep-D packed column (4 m × 1/8″) and quantified with a flame ionization detector. For water samples, we used Henry's law with measured headspace pressures and water volumes to convert headspace CH_4 concentrations to dissolved CH_4 concentrations. DIC concentrations were calculated from IRMS results, using known sample aliquot volumes and calibrated mass 44 (CO_2) peak areas.

We determined the dominant CH_4 production pathway in each soil profile using two stable isotope abundance metrics. We performed these analyses on the subset of total samples that were collected as water from the full depth of the thawed soil, where CH_4 isotopic compositions were unlikely to have been affected by oxidation, thus representing the values of CH_4 at the time of production. First, acetate cleavage and CO_2 reduction each yield CH_4 whose δ¹³C values fall within characteristic ranges (Whiticar *et al*., 1986; Hornibrook & Aravena, 2010). CH_4 produced by acetate cleavage typically has δ¹³C values between −65 and −50‰, whereas CH_4 from CO_2 reduction has δ¹³C values between −110 and −60‰. Second, the apparent fractionation factor ($\alpha_{DIC-CH4}$) is a measure of the isotope separation between CH_4 and co-occurring DIC (or CO_2) (Hines *et al*. 2008, Whiticar *et al*., 1986; Chanton *et al*. 2006):

$$\alpha_{DIC-CH_4} = \frac{\delta^{13}C - DIC + 1000}{\delta^{13}C - CH_4 + 1000}$$

$\alpha_{DIC-CH4}$ is termed *apparent* fractionation because it is not the fractionation factor for an individual process, but rather a composite metric describing kinetic fractionation during CO_2 reduction and acetate cleavage (Conrad, 2005) and equilibrium fractionation between carbonate species (Mook *et al*., 1974). $\alpha_{DIC-CH4}$ values vary along a continuum between environments where CH_4 is derived entirely from acetate cleavage and those where CH_4 is entirely a product of CO_2 reduction. Measured fractionation factors range from 1.007 to 1.027 for acetate cleavage and from 1.031 to 1.077 for CO_2 reduction (Conrad, 2005), so $\alpha_{DIC-CH4}$ values increase with increased importance of CO_2 reduction.

Statistical analyses

We analyzed CH_4 flux, R_{eco}, and deep pore water δ¹³C-CH_4 individually using linear mixed-effects models. We selected models based on Akaike information criterion (AIC) values with backward elimination of random and fixed effects, using significance cutoffs of $P < 0.1$ and $P < 0.05$ for random and fixed effects, respectively. *P*-values for random effects were assessed with likelihood ratio tests, and fixed-effect *P*-values were determined using *F*-tests based on Satterthwaite's approximation for denominator degrees of freedom. We calculated variance inflation factors, using a cutoff of 10 to avoid multicollinearity. Following fixed-effect selection, we tested all possible two-way interactions and then performed pairwise comparisons between individual positions, features, or months with Tukey's honest significant difference test, using degrees of freedom from Satterthwaite's approximation. All models included polygon and individual profile as possible random effects. For CH_4 flux and R_{eco} models, possible fixed effects included polygon type, position, sampling month, top 10 cm

soil moisture, and soil temperature at 10 cm depth. For the model of $\delta^{13}C\text{-}CH_4$, possible fixed effects were polygon type, position, and month. We conducted all analyses in R version 3.1.0 'Spring Dance' (October 4, 2014), using the packages LME4 (Bates *et al.*, 2014) for linear mixed-effects modeling, lmerTest (Kuznetsova *et al.*, 2014) for significance testing and model selection, and multcomp (Hothorn *et al.*, 2008) for pairwise comparisons.

Because CH_4 fluxes, R_{eco} measurements, and soil temperature measurements had skewed distributions, we log-transformed these variables for all statistical analyses. Model estimates and associated *P*-values reflect these transformed data. In all figures, however, we present nontransformed data to ease visual interpretation.

Results

CH_4 flux and ecosystem respiration

Surface CH_4 flux displayed clear patterns among polygon types and sampling dates (Fig. 1a, Table 1). When observations were averaged across the July–October 2013 season for each polygon type, mean CH_4 fluxes were 6.8 nmol m^{-2} s^{-1} from FHC polygons and 64 nmol m^{-2} s^{-1} from LC polygons. Averaged across all locations, mean CH_4 fluxes peaked in August, increasing from 37 to 45 nmol m^{-2} s^{-1} from July to August, and then decreased to 25 nmol m^{-2} s^{-1} in September and 18 nmol m^{-2} s^{-1} in October. LC polygons strongly influenced this temporal trend, their CH_4 flux dropping from 85 nmol m^{-2} s^{-1} in July and August to 39 nmol m^{-2} s^{-1} in October. During this period, FHC polygons' CH_4 flux decreased from only 15 to 3 nmol m^{-2} s^{-1}. To identify important predictors of CH_4 flux, we generated a suite of models including all possible combinations of predictor variables: polygon type, position, soil temperature at 10 cm depth, soil moisture from 0 to 10 cm depth, and/or sampling month. We then compared these models' AIC values to select the optimal model. The final model (AIC = 194.4) included polygon type ($P < 0.001$), position ($P < 0.01$), soil temperature ($P < 0.01$), and the interactions between type and position ($P < 0.001$), type and temperature ($P < 0.01$), and temperature and position ($P < 0.01$) as predictor variables (Table 2). Based on AIC values, neither soil moisture nor sampling month was included in the final model. With a significance cutoff of $P < 0.05$, CH_4 emissions were significantly different between all but three pairs of polygon features (Table 3). These three exceptions were FHC polygon centers and rims (0.51 and 0.54 nmol m^{-2} s^{-1}), LC polygon centers and troughs (88 and 87 nmol m^{-2} s^{-1}), and LC polygon rims and FHC polygon troughs (17 and 20 nmol m^{-2} s^{-1}). Soil temperature, a significant predictor of CH_4 flux, peaked at the time of peak emissions: July in LC polygons and August in FHC polygons (Figs 1 and S1).
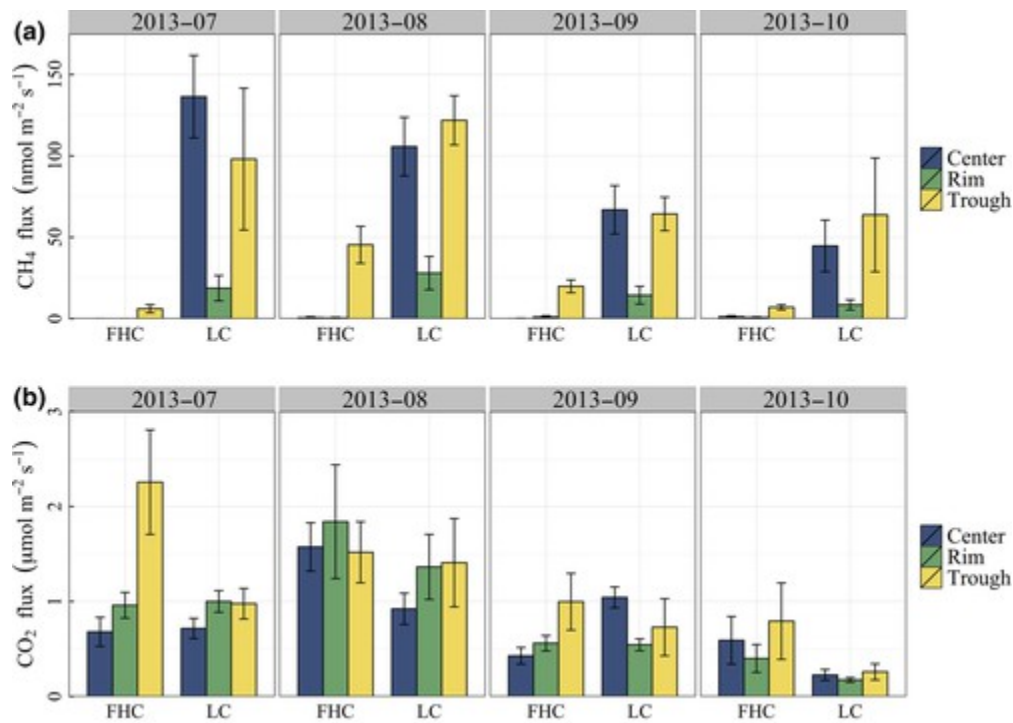
Figure 1

Greenhouse gas emissions, classified by polygon type, position, and measurement month. (a) Net CH$_4$ flux in nmol CH$_4$ m^{-2} s^{-1} and (b) ecosystem respiration in μmol CO$_2$ m^{-2} s^{-1} were measured from each feature of 4 flat/high-centered (FHC) and 3 low-centered (LC) polygons. Standard errors were calculated from field replicates.

Table 1. Mean surface greenhouse gas fluxes and deep pore water δ^{13}CH$_4$, averaged across all sampling dates for each polygon type and feature. Flux measurements were made from opaque static chambers in July, August, and September 2013 from 3 low-centered and 4 flat/high-centered polygons. δ^{13}CH$_4$ values were measured from water samples collected from the frost table in August 2012 and July–October 2013

Polygon type	Feature	CH$_4$ flux (nmol m^{-2} s^{-1})			CO$_2$ flux (μmol m^{-2} s^{-1})			δ^{13}CH$_4$ (‰)		
		Mean	SD	*n*	Mean	SD	*n*	Mean	SD	*n*
Low-centered	LC center	88.4	46	12	0.727	0.37	12	−52.3	4.7	12
	LC rim	17.4	13	12	0.771	0.54	12	−61.3	7.9	10
	LC trough	87.0	50	12	0.843	0.61	12	−59.1	6.8	10
	All LC positions	64.3	52	36	0.780	0.50	36	−57.2	7.4	32
Flat/high-centered	FHC center	0.505	1.0	17	0.805	0.59	17	−79.8	4.7	10
	FHC rim	0.538	0.95	16	0.940	0.81	16	−79.7	5.8	8
	FHC trough	19.6	20	16	1.39	0.93	16	−68.3	4.5	8
	All FHC positions	6.75	14	49	1.04	0.81	49	−76.2	7.2	26

Table 2. fixed effects included in linear mixed-effects models for CH$_4$ flux, CO$_2$ flux, and deep pore water δ^{13}CH$_4$. Optimal models were chosen based on AIC values

Model	Fixed effect	DF	F value	Pr > |F|
CH_4 flux (AIC = 168.8)	Polygon type	56.782	54.819	6.894e-10***
	$\log_{10}$(temperature)	56.405	10.729	0.001807**
	Position	51.832	6.052	0.004342**
	Type × position	21.902	15.157	7.377e-05***
	Type × $\log_{10}$ (temperature)	56.180	8.634	0.004778**
	Position × $\log_{10}$ (temperature)	56.926	5.763	0.005256**
CO_2 flux (AIC = 175.0)	Month	64.041	28.946	5.997e-12***
$\delta^{13}CH_4$ (AIC = 369.0)	Polygon type	18.515	71.717	8.694e-08***
	Position	19.038	2.536	0.1056001
	Month	40.126	8.906	3.034e-05***
	Type × position	18.529	9.856	0.0012151**
	Month × position	39.756	4.216	0.0009954***

Significance codes: 0 ***0.001 **0.01 *0.05 .1.

Table 3. Results of Tukey's honest significant difference test for linear mixed-effects models predicting CH_4 flux, CO_2 flux, and $\delta^{13}CH_4$. Each row summarizes a test for differences between two levels of a categorical predictor variable, with P-values < 0.05 indicating significant differences. P-values were calculated using Satterthwaite's approximation for degrees of freedom

Model	Predictor variable	Contrasted levels	t value	Pr > |t|
CH_4 flux	Type × position	LC center–FHC center	11.028	<0.001***
	Type × position	LC rim–FHC center	7.417	<0.001***
	Type × position	LC trough–FHC center	10.992	<0.001***
	Type × position	FHC rim–FHC center	−0.020	1.0000
	Type × position	FHC trough–FHC center	7.873	<0.001***
	Type × position	LC rim–LC center	−3.474	0.0229*
	Type × position	LC trough–LC center	−0.045	1.0000
	Type × position	FHC rim–LC center	−11.077	<0.001***
	Type × position	FHC trough–LC center	−3.745	0.0126*
	Type × position	LC rim–FHC rim	7.415	<0.001***
	Type × position	LC trough–FHC rim	11.037	<0.001***
	Type × position	FHC trough–FHC rim	7.907	<0.001***
	Type × position	LC trough–LC rim	3.431	0.0252*
	Type × position	FHC trough–LC rim	−0.031	1.0000
	Type × position	LC trough–FHC trough	3.698	0.0139*

Model	Predictor variable	Contrasted levels	t value	Pr > |t|
CO_2 flux	Sampling month	August 2013–July 2013	1.714	0.3251
	Sampling month	September 2013–July 2013	−2.482	0.0727
	Sampling month	October 2013–July 2013	−7.007	<0.001***
	Sampling month	September 2013–August 2013	−4.196	<0.001***
	Sampling month	October 2013–August 2013	−8.739	<0.001***
	Sampling month	October 2013–September 2013	−4.499	<0.001***
$\delta^{13}CH_4$	Position	Rim–center	0.427	0.90493
	Position	Trough–center	3.706	0.00515**
	Position	Trough–rim	3.365	0.01031*
	Sampling month	July 2013–August 2012	4.253	0.00116**
	Sampling month	August 2013–August 2012	3.407	0.01236*
	Sampling month	September 2013–August 2012	2.979	0.03674*
	Sampling month	October 2013–August 2012	2.846	0.05068
	Sampling month	August 2013–July 2013	−1.389	0.63596
	Sampling month	September 2013–August 2013	−1.178	0.76153
	Sampling month	October 2013–July 2013	−1.431	0.60908
	Sampling month	September 2013–August 2013	−0.012	1.00000
	Sampling month	October 2013–August 2013	−0.231	0.99934
	Sampling month	October 2013–September 2013	−0.190	0.99969

- Significance codes: 0 ***0.001 **0.01 *0.05 .1.

R_{eco} varied temporally, but did not vary significantly among locations (Fig. 1b, Table 1). The optimal model predicting R_{eco} (AIC = 175) included only sampling month ($P < 0.001$) as a significant fixed effect (Table 2). The highest R_{eco} fluxes were measured in July and August (1.1 and 1.5 µmol m^{-2} s^{-1}, not significantly different), then decreased between August and September to 0.71 µmol m^{-2} s^{-1} ($P < 0.001$), and decreased further from September to October to 0.44 µmol m^{-2} s^{-1} ($P < 0.001$) (Table 3). Notably, FHC polygon troughs had high R_{eco} in July relative to other sampling months and polygon features (Fig. 1b).

Dissolved gas concentrations

For all polygon features, CH$_4$ concentrations increased with depth in the soil to high concentrations at the frost table (Fig. 2a). These deep CH$_4$ concentrations were highest in features with saturated or inundated surface soils: LC polygon centers and troughs of both polygon types. Even in FHC polygon centers and rims, however, where net surface CH$_4$emissions were near zero, deep CH$_4$ concentrations were >100 μM. Particularly in polygon rims and troughs, between-type differences in surface CH$_4$ fluxes were not mirrored by deep CH$_4$concentrations. Instead, patterns in surface flux corresponded more closely with concentrations at 10 and 20 cm. Of the six polygon features examined, the two with lowest net CH$_4$ fluxes – centers and rims of FHC polygons – had average 10 cm CH$_4$ concentrations only slightly greater than zero, at 1.3 and 1.0 μM, respectively. Among the remaining four features, the two with highest CH$_4$ flux – centers and troughs of LC polygons – had high CH$_4$concentrations at all depths. Between LC polygon rims and FHC polygon troughs, which had intermediate CH$_4$ flux rates, LC polygon rims had both higher CH$_4$ emissions and higher 20 cm CH$_4$ concentrations. The apparent disconnect between deep dissolved CH$_4$ and surface emissions suggests that three possible mechanisms underlie differences in net CH$_4$ fluxes: (1) different CH$_4$ production rates in shallow soil, (2) different CH$_4$ transport rates from deep soils to the atmosphere, and/or (3) different oxidation rates in shallow soils.
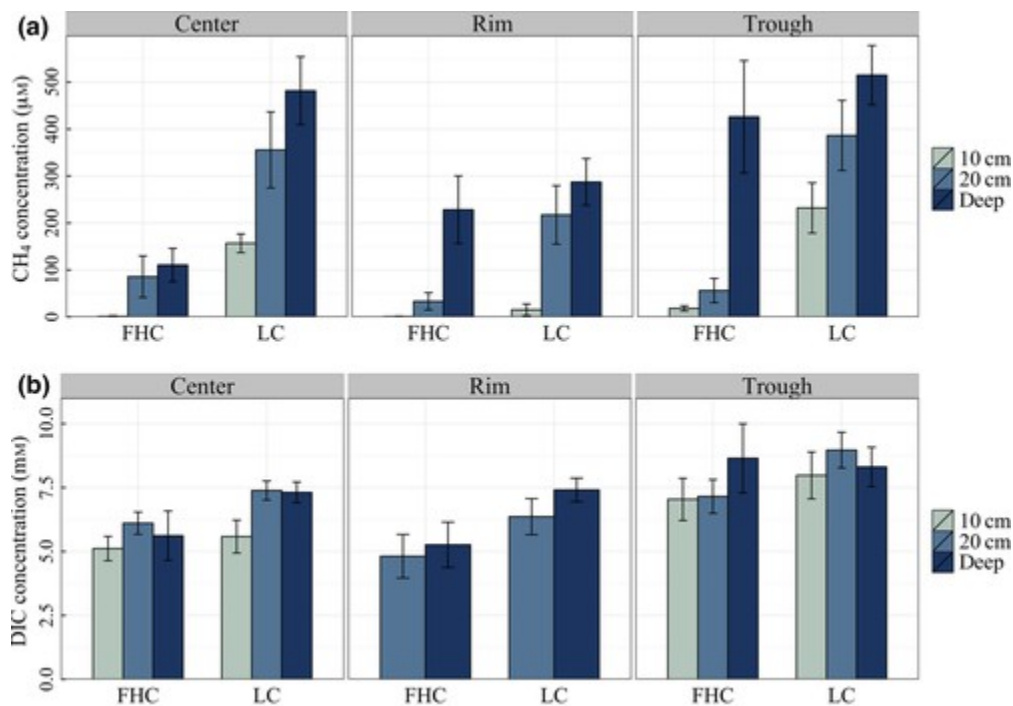

Figure 2

Concentration depth profiles of (a) dissolved CH$_4$ and (b) DIC in soil pore water. Results are classified by polygon type, position, and depth from the soil surface. Mean concentrations and standard errors include water samples collected in August 2012 and monthly from July–October 2013 from 4 flat/high-centered and 3 low-centered polygons. Data presented here include water samples only and do not include gas samples.

DIC concentrations varied less than did those of dissolved CH_4 (Fig. 2b). DIC sources may include *in situ* CO_2 production by root respiration, aerobic or anaerobic respiration, fermentation, or methanogenesis, or transport to the sampling location by diffusion or advection. DIC sinks are primarily diffusion or advection in soil pore water or CH_4 production via CO_2 reduction. Mean DIC concentrations generally increased with depth, but in FHC polygon centers, LC polygon centers, and LC polygon rims, the highest DIC concentrations were measured at 20 cm, indicating higher CO_2 production at 20 cm than at the frost table.

Methane production pathways

^{13}C abundances in CH_4 and DIC from deep pore water were used to compare CH_4 production pathways among polygon types and positions (Fig. 3), following published approaches (Whiticar *et al*., 1986; Hornibrook *et al*., 1997; Conrad, 2005; Hornibrook & Aravena, 2010). Because these samples were collected from deep, saturated soils with limited oxygen availability (Lipson *et al*., 2012), their $\delta^{13}C$ values reflect CH_4 at the time of production, without isotopic fractionation due to bacterial aerobic CH_4 oxidation. Similarly, we assumed anaerobic CH_4 oxidation had a negligible effect on measured CH_4 isotopes. While anaerobic CH_4oxidation has been demonstrated in terrestrial soils, concurrent CH_4 production is thought to proceed far more rapidly, particularly in highly methanogenic soils (Blazewicz *et al*., 2012; Gupta *et al*., 2013). Additionally, we assumed measured $\delta^{13}C$ values of CH_4 were not affected by kinetic fractionation during transport through the soil profile. Ebullition and advection through plant aerenchyma tissues are nonfractionating processes, but isotopic fractionation may occur during diffusive transport through plants (Popp *et al*., 1999; Chanton, 2005; Hornibrook, 2009). It is possible that such fractionation may have occurred, isotopically enriching residual soil CH_4. However, studies have shown that this fractionation occurs primarily within the plant tissues themselves, creating a $\delta^{13}C$ gradient between heavier CH_4within plant aerenchyma and lighter CH_4 emitted from plant tissues to the atmosphere (Chanton *et al*., 1992a,b; Tyler *et al*., 1997), with little effect on soil pore space $\delta^{13}C$-CH_4.
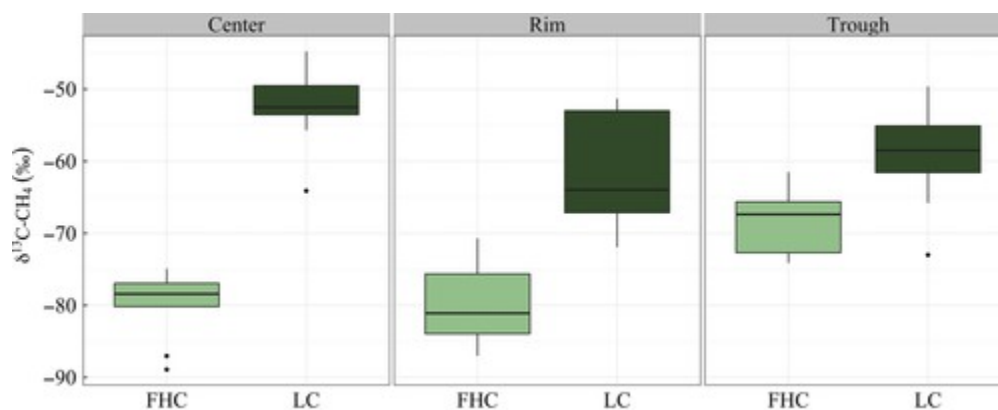

Figure 3

Open in figure viewer PowerPoint

$\delta 13C$ of CH_4 in water samples collected from the frost table. Data are classified by polygon type and position and include all sampling dates from August 2012 and July–October 2013. Box plots indicate median and first and third quartiles, with whiskers extending to the farthest values within 1.5 times the upper and lower quartiles. Outliers beyond this range are shown as points.

Including all sampling dates, deep pore water $\delta^{13}C$-CH_4 values were 17‰ enriched from LC polygons relative to FHC polygons ($P << 0.001$), and significant interactions were found between polygon type and position ($P < 0.01$) and between position and sampling month ($P < 0.001$). Between-type differences in $\delta^{13}C$-CH_4 were most pronounced for centers and least pronounced for troughs (Table 2), and $\delta^{13}C$-CH_4 was significantly higher in all 2013 months relative to August 2012, but did not change significantly over the 2013 season (Table 3). Including all sampling dates, 12 of 12 samples from LC polygon centers (mean $\delta^{13}C$-CH_4 = −52.3‰) and 8 of 10 samples from LC polygon troughs (mean $\delta^{13}C$-CH_4 = −59.1‰) had $\delta^{13}C$-CH_4 values within the range characteristic of acetate cleavage, −65 to −50‰ (Table 1) (Whiticar et al., 1986; Hornibrook & Aravena, 2010). In contrast, 10 of 10 samples from FHC polygon centers (mean $\delta^{13}C$-CH_4 = −79.8‰), 8 of 8 samples from FHC polygon rims (mean $\delta^{13}C$-CH_4 = −79.7‰), and 6 of 8 samples from FHC troughs (mean $\delta^{13}C$-CH_4 = −68.3‰) had $\delta^{13}C$-CH_4 values within the range typical of CO_2 reduction, −110 to −60‰ in an ecosystem with C_3 vegetation. $\delta^{13}C$-CH_4 values from LC polygon rims (mean $\delta^{13}C$-CH_4 = −61.3‰) were divided among the plausible ranges of both pathways, with six samples between −50 and −65‰ and 4 samples below −65‰, with both methanogenic processes likely operating concurrently (Whiticar, 1999).

The difference in $\delta^{13}C$ between co-occurring CH_4 and DIC, referred to as the apparent fractionation factor, $\alpha_{DIC\text{-}CH4}$, provides an additional line of evidence that the dominant methanogenic pathways differed between polygon types. As shown in cross-plots of $\delta^{13}C$-DIC vs. $\delta^{13}C$-CH_4 (Fig. 4), $\alpha_{DIC\text{-}CH4}$ values displayed the same patterns as $\delta^{13}C$-CH_4, with acetate cleavage more important in LC than in FHC polygons. $\alpha_{DIC\text{-}CH4}$ values from polygon centers and rims showed clear separation between LC and FHC polygons, with values clustering around 1.07 for FHC polygons and around 1.04–1.05 for LC polygons. Troughs displayed some clustering of $\alpha_{DIC\text{-}CH4}$ values for each polygon type, but this separation between $\alpha_{DIC\text{-}CH4}$ ranges of LC and FHC polygons was smaller than in centers and rims.
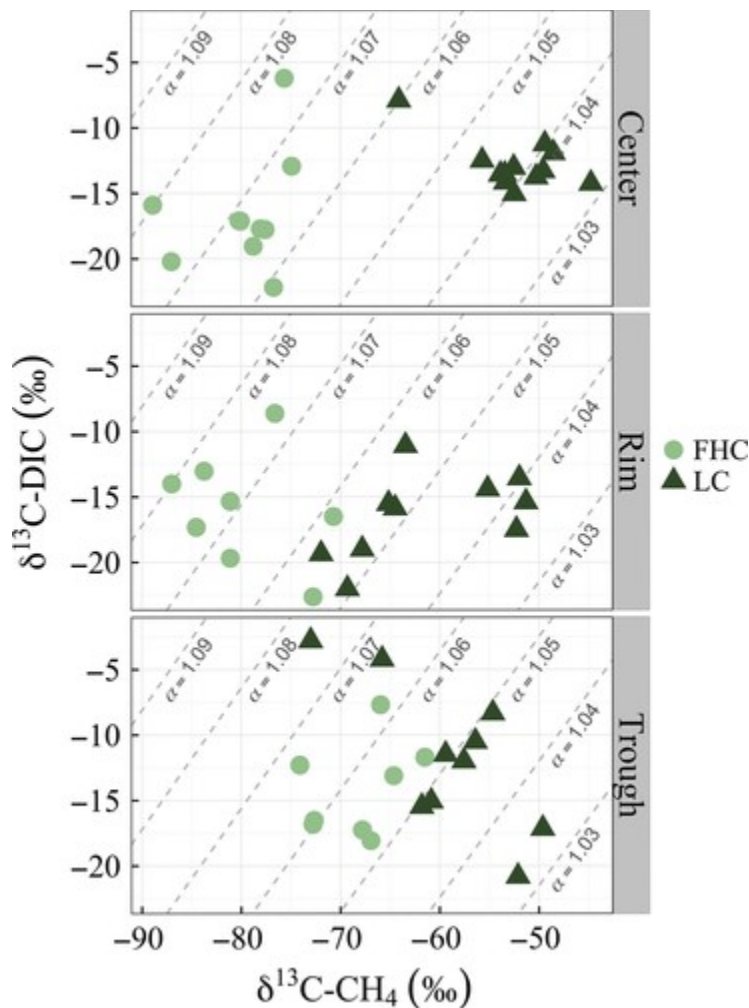
Figure 4

Cross-plots showing δ¹³C-DIC and δ¹³C-CH₄ of individual soil pore water or gas samples. Dark triangles are flat/high-centered (FHC) polygons, and light circles are low-centered (LC) polygons. Dashed diagonal lines show equal fractionation between CH₄ and co-occurring DIC, with the fractionation factor (α) decreasing from top left to bottom right of each panel.

Apparent fractionation factors between CH₄ and CO₂ below 1.055 are generally thought to indicate acetate cleavage, while values above 1.065 result from CO₂ reduction (Conrad, 2005). In this analysis, δ¹³C was measured from bulk DIC rather than CO₂. Because of equilibrium isotopic fractionation between dissolved CO₂ and bicarbonate (Mook *et al.*, 1974), our calculated $\alpha_{DIC\text{-}CH4}$ values may thus be slightly higher than values calculated from δ¹³C-CO₂. At the acidic pH range typical of this study site (Zona *et al.*, 2011), H₂CO₃ is the dominant carbonate species, so we would expect only small ¹³C differences between CO₂ and total DIC. Even so, we conducted an empirical sensitivity analysis to assess the potential for carbonate equilibrium fractionation to influence $\alpha_{DIC\text{-}CH4}$. We measured both δ¹³C-DIC and vial headspace δ¹³C-CO₂ from a subset of deep pore water samples, finding that isotope separation ranged from 0.2 to 5.7‰. To account for the maximum possible influence on $\alpha_{DIC\text{-}CH4}$, we applied a 5.7‰ correction to δ¹³C-DIC values to generate a conservative uncertainty band, which decreased calculated $\alpha_{DIC\text{-}CH4}$ values by 0.0065. Including this range of error, $\alpha_{DIC\text{-}CH4}$ values above 1.059 can be interpreted to indicate CO₂ reduction. With these considerations, we still found acetate cleavage

dominated all LC polygon features. CO_2 reduction dominated in FHC polygons features, with acetate cleavage more important in FHC polygon troughs than in other FHC polygon features.

$\delta^{13}C$ depth profiles

Depth profiles of $\delta^{13}C\text{-}CH_4$ displayed spatial patterns similar to those of surface fluxes (Fig. 5). $\delta^{13}C$ abundance in pore space CH_4 increased toward the soil surface in four of the six polygon features, a depth trend that would be expected from CH_4 oxidation in shallow soil layers. Among these four features, the difference in mean $\delta^{13}C\text{-}CH_4$ between 10 cm and the frost table was greatest in FHC polygon rims ($\Delta\delta^{13}C$ = 18.4‰) and FHC polygon centers ($\Delta\delta^{13}C$ = 13.1‰), where surface CH_4 flux rates were lowest. By comparison, LC polygon rims and FHC polygon troughs had both lower surface CH_4 fluxes and lower $\delta^{13}C\text{-}CH_4$ depth gradients ($\Delta\delta^{13}C$ = 7.9 and 5.5‰, respectively). The only two features that did not display this $\delta^{13}C\text{-}CH_4$ depth gradient were those with the highest surface CH_4 fluxes: LC polygon centers and LC polygon troughs. There, the highest $\delta^{13}C\text{-}CH_4$ values occurred at 20 cm depth. We note that these two features were inundated at all times, with mean water depths of 8.0 ± 2.1 and 6.7 ± 1.6 cm, respectively (data not shown), so their 10 cm samples were collected near the sediment surface or from standing water.
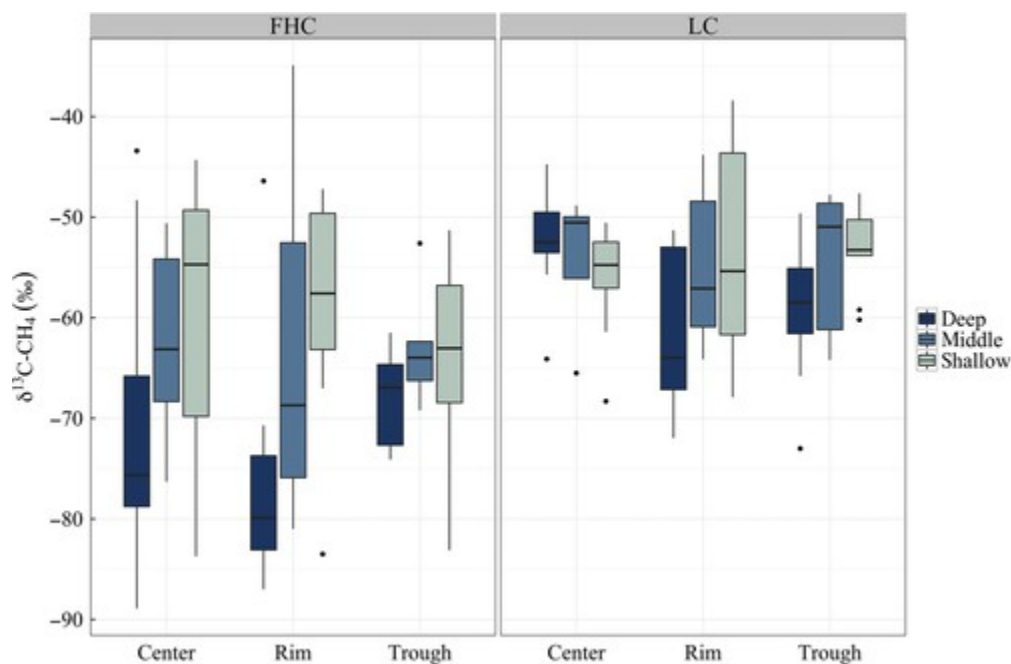

Figure 5

Depth profiles of $\delta^{13}CH_4$ within the soil pore space. Data are classified by polygon type, position, and depth from the soil surface. Shallow samples were collected from 10 cm below the surface, and deep samples were collected from the frost table. The middle depth increment includes samples collected from 20 cm below the surface if total thaw depth was >20 cm. If a soil profile's thaw depth was ≤20 cm, any sample deeper than 10 cm was classified as deep.

Discussion

High-latitude soils are a large source of atmospheric CH_4 (Whalen & Reeburgh, 1992; McGuire *et al.*, 2012; Mastepanov *et al.*, 2013). Current Earth system models project that Arctic tundra CH_4 emissions will increase

with climate change (Koven *et al.*, 2011; Lawrence *et al.*, 2015; Schuur *et al.*, 2015). However, landscape-scale processes may influence CH_4 emissions in ways that these models are only beginning to represent. To better understand the relationship between landscape change and CH_4 dynamics, we combined measurements of surface CH_4 flux with subsurface CH_4 concentration and $\delta^{13}C$ profiles to assess (1) how CH_4 production and consumption processes vary with permafrost degradation and microtopography, and (2) how these subsurface processes relate to net CH_4 and CO_2 fluxes. Beyond confirming that CH_4 fluxes from wetter, LC polygons are higher than from drier, FHC polygons, we found that the dominant CH_4 production pathway differed between polygons types, with acetate cleavage more important in high-production locations. In addition, CH_4 emissions decreased with permafrost degradation, beyond the degree that would be expected from moisture changes alone.

CH_4 fluxes were on average ~10 times higher from LC polygons than from FHC polygons (Table 1). While soil moisture (Fig. S2) mirrored the positive moisture–CH_4 relationship that has been documented in Arctic polygon tundra (Sachs *et al.*, 2010; Kim, 2015), other tundra types (Torn & Chapin, 1993; Christensen *et al.*, 1995; McCalley *et al.*, 2014), and thermokarst landscapes (Walter *et al.*, 2007; Desyatkin *et al.*, 2009), the differences in CH_4 flux between polygon types were greater than variations in moisture or temperature alone could explain. Specifically, we found that polygon type, geomorphic position, and soil temperature were the only significant main effects in our optimal model of CH_4 flux (Table 2). Soil moisture did not emerge as a significant predictor variable, but this result does not imply that soil moisture and CH_4 flux were unrelated. Instead, the predictor variables polygon type and position accounted for soil moisture information, along with additional explanatory power that modified the soil moisture–CH_4 flux relationship. Pairwise comparisons between positions within the two polygon types highlight the kind of unexpected feature-level differences that underlie this model result (Table 3). Rims from LC vs. FHC polygons had a 30-fold difference in mean surface CH_4 flux, in spite of comparable temperatures, thaw depths, and moisture contents (Figs S1 and S2). Similarly, FHC polygon troughs had only ~20% the CH_4 emissions of LC polygon troughs, with nearly equal soil moisture. In contrast to CH_4 flux, we found that surface CO_2 flux, equivalent to R_{eco}, depended primarily on sampling month, a variable that captures temporal changes in temperature, plant productivity, and microbial community. The R_{eco} model did not find polygon type or position to be significant predictor variables, indicating that carbon availability and turnover did not map strongly to microtopography or permafrost degradation and thus cannot account for observed CH_4 flux variations.

The dominant CH_4 production pathway differed between high- and low-emission areas. Based on $\delta^{13}C$-CH_4 values, CH_4 production in locations with high surface emissions (e.g., LC polygons and FHC troughs) occurred primarily by acetate cleavage, whereas production in areas with low emissions (FHC polygons) was dominated by CO_2 reduction (Fig. 3, Table 2). The relationship between surface CH_4 flux and deep pore water $\delta^{13}C$-CH_4 held not only between polygon types but also among positions within each polygon type. We observed the highest and lowest $\delta^{13}C$-CH_4 values in features with the greatest and least CH_4 emissions, respectively (LC polygon centers and troughs vs. FHC polygon centers and rims).

This analysis assumes that measured $\delta^{13}C$-CH_4 values reflect *in situ* production, with most sampled CH_4 produced in the soil column, not imported by lateral transport. Supporting evidence includes low flow rates

(Liljedahl *et al*., 2012) relative to *in situ* cycling rates within LC polygons and low CH_4 concentrations in the runoff of FHC polygon centers.

In addition to our observed relationship between surface CH_4 flux rates and subsurface $\delta^{13}C$-CH_4 values, several lines of evidence suggest that acetate cleavage is correlated with higher production rates. Acetate cleavage dominates methanogenesis when organic matter is abundant and surface fluxes are high (Galand *et al*., 2010; Hershey *et al*., 2014), whereas CO_2 reduction is more important in systems with low organic matter inputs, abundant terminal electron acceptors, and low surface flux rates, such as sulfate-rich marine sediments (Oremland & Taylor, 1978; Crill & Martens, 1983; Whiticar *et al*., 1986). Similarly, laboratory incubations of high-latitude soils have found higher rates of CH_4 production when acetate cleavage rather than CO_2 reduction dominates (Kotsyurbenko *et al*., 2007; Liebner *et al*., 2015). Moreover, theoretical reaction stoichiometries also predict acetate cleavage will dominate CH_4 production unless electron flow to methanogens is limited by competition or biochemical inhibition (Conrad, 1999; Ye *et al*., 2012; Bridgham *et al*., 2013). Applied to our results, this relationship between CH_4 production rate, CH_4 flux, and $\delta^{13}CH_4$ suggests that CH_4 production rate was an important control on surface CH_4 flux. In locations with high surface CH_4 emissions and less negative $\delta^{13}CH_4$ values such as LC polygon centers and troughs, CH_4 was produced rapidly via acetate cleavage. In FHC polygon centers and rims, acetate oxidation using dissolved oxygen, iron (III), or sulfate may have limited acetate availability to methanogens, leading to low rates of methanogenesis by CO_2 reduction. Thus, we infer that a direct control on net CH_4 emissions, CH_4 production rate, maps predictably to polygonal tundra features.

Previous studies have noted that as much as 90% of CH_4 production is oxidized in the soil profile (King, 1992; Le Mer & Roger, 2001), so biotic oxidation can be an important determinant of surface CH_4 flux rates. Based on subsurface CH_4 concentrations, flux rates, and $\delta^{13}C$-CH_4 depth profiles (e.g., Figs 3 and 5), we find that oxidation plays an important role in some but not all geomorphic positions, with the greatest degree of oxidation in FHC polygon centers and rims and the least influence of oxidation in LC polygon centers and troughs. Deep subsurface CH_4 concentrations indicate that substantial methanogenesis occurred at all locations, even those with minimal net surface emissions. Mediating the relationship between this subsurface production and surface emissions, steep depth profiles of $\delta^{13}C$-CH_4 show that CH_4 oxidation attenuated this gross production in low-emission sites.

While other studies have used $\delta^{13}C$-CH_4 depth profiles to derive quantitative estimates of CH_4 oxidation, we chose to use this dataset to infer qualitative differences in CH_4 oxidation (Fig. 5). If the $\delta^{13}C$-CH_4 of production and the oxidation fractionation factor were known or assumed, $\delta^{13}C$-CH_4 depth profiles could be used to quantitatively calculate fractional CH_4 oxidation (Liptay *et al*., 1998; Popp *et al*., 1999; Corbett *et al*., 2013). In high-latitude wetlands, however, methanogenic pathway and thus its isotopic signature can change with depth, due to shifts in substrate availability, temperature, and pH (Hornibrook *et al*., 1997; Popp *et al*., 1999; Hornibrook & Aravena, 2010). Further, documented fractionation factors for CH_4 oxidation range from 1.003 to 1.031, varying by 0.011 within tundra soils alone (King *et al*., 1989; Happell *et al*., 1994; Chanton *et al*., 2005).

Synthesizing isotope, flux, and moisture data, two clear regimes emerge relating soil moisture, CH_4 production, and CH_4 oxidation to net CH_4 emissions (Fig. S3). First, hydrologically isolated features with persistently low soil

moisture, FHC polygon centers and rims, were dominated by CO_2 reduction and had steep $\delta^{13}C$-CH_4 depth gradients, indicating that both low production and high oxidation contributed to low surface emissions. Second, persistently inundated features, LC polygon centers and troughs, were dominated by acetate cleavage with small or negative $\delta^{13}C$-CH_4 depth gradients. There, high CH_4 production and low CH_4 oxidation yielded high surface emissions. The two remaining features, FHC polygon troughs and LC polygon rims, do not fit clearly into either of these regimes. With roughly equal surface CH_4 emissions but clear soil moisture differences, these features had notable differences in CH_4 production and CH_4 oxidation. Specifically, LC polygon rims had higher deep $\delta^{13}C$-CH_4 values and steeper $\delta^{13}C$-CH_4 profiles than did FHC polygon troughs, indicating higher rates of both production and oxidation. With comparable, moderate CH_4 fluxes but different soil moisture contents and subsurface processes, these are key locations in the landscape where models based on soil moisture might produce the wrong results, highlighting the importance of other upstream controls on CH_4 production and oxidation.

The two proximate controls on surface CH_4 flux – subsurface CH_4 production and oxidation – are influenced by upstream controls that link landscape processes to microbial activity. Two such upstream controls stand out as particularly important for the relationship between permafrost degradation and CH_4 emissions. First, vegetation influences CH_4 production and oxidation through substrate availability, gas transport, and its influence on subsurface pH, temperature, active layer depth, and other factors (Popp *et al.*, 1999; Chanton, 2005), as seen in a positive relationship between surface CH_4 flux and sedge cover or vegetation stature in wet tundra (Schimel, 1995; Ström *et al.*, 2003; Von Fischer *et al.*, 2010; Olefeldt *et al.*, 2013). Based on vegetation surveys adjacent to our plots (Table S1), we find the same qualitative relationship between surface CH_4 emissions and plant community composition or canopy height. In particular, percent cover of *Carex aquatilis*, a sedge with aerenchyma known to transport CH_4 (Popp *et al.*, 1999; Ström *et al.*, 2003; Chanton, 2005), has a spatial pattern matching our stable isotope and surface flux measurements. *Carex* cover and vegetation canopy height are high in LC polygon centers and troughs, intermediate in LC polygon rims and FHC polygon troughs, and low in FHC polygon centers and rims. The observed transition to lower-stature, less *Carex*-dominated vegetation across the permafrost degradation gradient suggests that vegetation changes may play an important role in determining the response of CH_4 emissions to future warming-induced landscape changes.

A second upstream control, soil oxygen status, simultaneously controls substrate availability to methanogens (Chapin *et al.*, 2011), electron acceptor oxidation state (Cappellen & Wang, 1996), and CH_4 consumption rate (Mancinelli, 1995). In unsaturated soils such as FHC polygon centers and rims, oxygen is readily available, inhibiting CH_4 production and promoting oxidation. In saturated soils, the abundance of dissolved oxygen and other electron accepting species depends on the combined influence of hydrology and geochemistry (Fiedler *et al.*, 2004; Herndon *et al.*, 2015b). Differences in hydrology and redox-active geochemical species between microtopographic features (Newman *et al.*, 2015) correspond to the CH_4 process differences we observed. Important redox indicators, pore water dissolved oxygen (DO) and sulfate concentrations are higher in high-centered polygon centers and troughs than in any low-centered polygon feature (Newman *et al.*, 2015), and modeled runoff rates from high-centered polygons are nearly twice as high as from

low-centered polygons (Liljedahl *et al.*, 2012). These geochemical and hydrological factors may explain the low CH_4 emissions from FHC troughs relative to other saturated or inundated features. Higher flow into high-centered polygon troughs likely imports DO, which is used to oxidize organic substances, iron, and CH_4 produced at depth where more favorable electron acceptors are depleted. (Iron in particular has been shown to be an important redox control on CH_4 production at this site (Herndon *et al.*, 2015a; Miller *et al.*, 2015), whereas sulfate is less likely to play an important role in anaerobic decomposition at this site because it is present only in low abundance.) Thus, we hypothesize that through its influence on redox, hydrology is an important control on CH_4 production and oxidation, leading to differences in CH_4 emissions among saturated polygon features.

We have shown that CH_4 production, CH_4 oxidation, and net CH_4 emissions depend not only on soil moisture and temperature, but also on microtopographic position along a permafrost degradation gradient. Importantly, redox status and vegetation can vary among sites of similar inundation, influencing substrate availability to methanogens and CH_4 availability to methanotrophs. Indeed, as thermokarst affects hydrology and geochemistry through physical subsidence, it also influences vegetation, with rapid changes in species dominance following drainage and subsidence events (Camill *et al.*, 2001; Christensen *et al.*, 2004; Schuur *et al.*, 2007). In addition, soil carbon chemistry and stocks vary among polygon types and features (Ping *et al.*, 1998; Bockheim *et al.*, 1999; Minke *et al.*, 2009; Zona *et al.*, 2011), as thaw-induced erosion redistributes stocks and alters conditions for organic matter accumulation (Anthony *et al.*, 2014; Godin *et al.*, 2014).

The geomorphic consequences of permafrost degradation depend on the quantity and organization of subsurface ice (Ulrich *et al.*, 2014), overall topography (Czudek & Demek, 1970; Schuur *et al.*, 2007; Godin *et al.*, 2014), and other site-specific properties (Jorgenson *et al.*, 2013). In some instances, permafrost thaw creates lakes or wetlands (Christensen *et al.*, 2004; Wickland *et al.*, 2006; Sannel & Kuhry, 2011; Johnston *et al.*, 2014; Klapstein *et al.*, 2014; Natali *et al.*, 2015), but in other instances it drains these features (Yoshikawa & Hinzman, 2003; Smith, 2005; Schuur *et al.*, 2007). The former of these two outcomes has received more attention with respect to CH_4 emissions, but both have important – and different – implications. Whereas research in other Arctic tundra types has found increased CH_4 emissions with permafrost thaw due to increased inundation following subsidence (Wickland *et al.*, 2006; Johnston *et al.*, 2014; McCalley *et al.*, 2014; Natali *et al.*, 2015), we report opposite trends in both CH_4 flux and water status. Overall, the influence of warming on local CH_4 emissions will depend strongly on the interaction between temperature and hydrology. This interaction may change with time; short-term thaw-driven CH_4 flux increases may be followed by longer-term drainage and drying. Given uncertainties regarding polygon succession processes (Ellis *et al.*, 2008), we cannot predict the degree to which climate warming and permafrost thaw will shift low-centered polygon terrain to drained, flat-centered and/or high-centered polygons. It is known, however, that such a directional change is possible, shifting polygon landscapes to drier, more high-centered equilibria. This change has recently been observed (Jorgenson *et al.*, 2006; Fortier *et al.*, 2007; Godin *et al.*, 2014), suggesting that continued warming should drive more such landscape transitions. To illustrate the potential magnitude of such changes, if 25% of our study site area's low-centered polygons transitioned to flat-centered and high-centered

polygons, a change consistent with projected changes in Alaska (Jorgenson *et al*., 2006), our results imply a 19% decrease in local CH_4 emissions.

In conclusion, our results demonstrate a local reduction in CH_4 emissions with permafrost degradation, counter to most published studies. We find that CH_4 production and surface flux depend categorically on polygon type, even after accounting for soil moisture differences. These findings show that changes in Arctic CH_4 emissions will be site-specific in sign and magnitude, depending on local geochemistry, topography, and patterns of subsidence. Changes in subsurface ice influence hydrological flows, geochemical redistribution, and physical soil carbon uplift, which in turn affect microbial community and activity as well as vegetation, substrate quantity, accessibility, and chemistry, and electron acceptor availability (Christensen *et al*., 2004; Fiedler *et al*., 2004; Fortier *et al*., 2007; Lantz *et al*., 2009; Hodgkins *et al*., 2014; McCalley *et al*., 2014). These processes control CH_4 emissions directly and indirectly, yet are rarely explicit in conceptual frameworks for sampling and understanding CH_4 fluxes or in numerical models that represent them. Despite common predictions for increased Arctic CH_4 emissions, this study documents a landscape-scale mechanism by which the widespread permafrost thaw predicted throughout the Arctic could result in localized decreases in CH_4 emissions.

Acknowledgments

References

1.   Anthony KMW, Zimov SA, Grosse G *et al*. (2014) A shift of thermokarst lakes from carbon sources to sinks during the Holocene epoch. *Nature*, **511**, 452–456.

2.   Avis CA, Weaver AJ, Meissner KJ (2011) Reduction in areal extent of high-latitude wetlands in response to permafrost thaw. *Nature Geoscience*, **4**, 444–448.

3.   Bates D, Maechler M, Bolker BM, Walker S (2014) lme4: Linear mixed-effects models using Eigen and S4. R package version 1.1-7.

4.   Billings WD, Peterson KM (1980) Vegetational change and ice-wedge polygons through the thaw-lake cycle in Arctic Alaska. *Arctic and Alpine Research*, **12**, 413–432.

5.   Black RF (1964) *Gubik Formation of Quaternary Age in Northern Alaska*. United States Geological Survey, Washington, DC.

6.   Blazewicz SJ, Petersen DG, Waldrop MP, Firestone MK (2012) Anaerobic oxidation of methane in tropical and boreal soils: ecological significance in terrestrial methane cycling. *Journal of Geophysical Research: Biogeosciences (2005–2012)*, **117**, G02033.

7.   Bockheim JG, Everett LR, Hinkel KM, Nelson FE, Brown J (1999) Soil organic carbon storage and distribution in Arctic tundra, Barrow, Alaska. *Soil Science Society of America Journal*, **63**, 934–940.

8.   Bohn TJ, Lettenmaier DP, Sathulur K, Bowling LC, Podest E, McDonald KC, Friborg T (2007) Methane emissions from western Siberian wetlands: heterogeneity and sensitivity to climate change. *Environmental Research Letters*, **2**, 045015.

9.   Bridgham SD, Cadillo-Quiroz H, Keller JK, Zhuang Q (2013) Methane emissions from wetlands: biogeochemical, microbial, and modeling perspectives from local to global scales. *Global Change Biology*, **19**, 1325–1346.

10.   Brown J (1967) Tundra soils formed over ice wedges, northern Alaska. *Soil Science Society of America Journal*, **31**, 686–691.

11.   Brown J, Miller PC, Tieszen LL, Bunnell F (1980) *An Arctic ecosystem?: the coastal tundra at Barrow, Alaska*. Dowden, Hutchinson and Ross, Inc., Stroudsburg, PA.

12.   Camill P, Lynch JA, Clark JS, Adams JB, Jordan B (2001) Changes in biomass, aboveground net primary production, and peat accumulation following permafrost thaw in the boreal peatlands of Manitoba, Canada. *Ecosystems*, **4**, 461–478.

13.   Cappellen PV, Wang Y (1996) Cycling of iron and manganese in surface sediments; a general theory for the coupled transport and reaction of carbon, oxygen, nitrogen, sulfur, iron, and manganese. *American Journal of Science*, **296**, 197–243.

14.   Chanton JP (2005) The effect of gas transport on the isotope signature of methane in wetlands. *Organic Geochemistry*, **36**, 753–768.

15.   Chanton J, Liptay K (2000) Seasonal variation in methane oxidation in a landfill cover soil as determined by an *in situ* stable isotope technique. *Global Biogeochemical Cycles*, **14**, 51–60.

16.   Chanton JP, Martens CS, Kelley CA, Crill PM, Showers WJ (1992a) Methane transport mechanisms and isotopic fractionation in emergent macrophytes of an Alaskan tundra lake. *Journal of Geophysical Research: Atmospheres*, **97**, 16681–16688.

17.   Chanton JP, Whiting GJ, Showers WJ, Crill PM (1992b) Methane flux from Peltandra virginica: stable isotope tracing and chamber effects. *Global Biogeochemical Cycles*, **6**, 15–31.

18.   Chanton JP, Chasar LC, Glaser P, Siegel D (2005) Carbon and hydrogen isotopic effects in microbial methane from terrestrial environments. Chapter 6. In: *Stable Isotopes and Biosphere‑Atmosphere Interactions*, *Physiological Ecology Series*, (eds Flanagan LB, Ehleringer JR, Pataki DE), pp. 85–105. Elsevier Academic Press, San Diego, CA.

19.   Chanton JP, Fields D, Hines ME (2006) Controls on the hydrogen isotopic composition of biogenic methane from high-latitude terrestrial wetlands. *Journal of Geophysical Research: Biogeosciences*, **111**, G04004.

20.   Chapin FS III, Matson PA, Vitousek P (2011) *Principles of Terrestrial Ecosystem Ecology*. (2nd edn). Springer Science & Business Media, New York, NY.

21.   Christensen TR, Jonasson S, Callaghan TV, Havström M (1995) Spatial variation in high-latitude methane flux along a transect across Siberian and European tundra environments. *Journal of Geophysical Research: Atmospheres*, **100**, 21035–21045.

22.   Christensen TR, Johansson T, Åkerman HJ *et al*. (2004) Thawing sub-arctic permafrost: effects on vegetation and methane emissions. *Geophysical Research Letters*, **31**, L04501.

23.   Conrad R (1999) Contribution of hydrogen to methane production and control of hydrogen concentrations in methanogenic soils and sediments. *FEMS Microbiology Ecology*, **28**, 193–202.

24.   Conrad R (2005) Quantification of methanogenic pathways using stable carbon isotopic signatures: a review and a proposal. *Organic Geochemistry*, **36**, 739–752.

25.   Corbett JE, Tfaily MM, Burdige DJ, Cooper WT, Glaser PH, Chanton JP (2013) Partitioning pathways of CO_2 production in peatlands with stable carbon isotopes. *Biogeochemistry*, **114**, 327–340.

26.   Corbett JE, Tfaily MM, Burdige DJ, Glaser PH, Chanton JP (2015) The relative importance of methanogenesis in the decomposition of organic matter in northern peatlands. *Journal of Geophysical Research: Biogeosciences*, **120**, 2014JG002797.

27.   Crill PM, Martens CS (1983) Spatial and temporal fluctuations of methane production in anoxic coastal marine sediments. *Limnology and Oceanography*, **28**, 1117–1130.

28.   Czudek T, Demek J (1970) Thermokarst in Siberia and its influence on the development of lowland relief. *Quaternary Research*, **1**, 103–120.

29.   Desyatkin AR, Takakai F, Fedorov PP, Nikolaeva MC, Desyatkin RV, Hatano R (2009) CH_4 emission from different stages of thermokarst formation in Central Yakutia, East Siberia. *Soil Science and Plant Nutrition*, **55**, 558–570.

30.   Donner N, Karpov NS, de Klerk P, Joosten H (2007) Distribution, diversity, development and dynamics of polygon mires: examples from Northeast Yakutia (Siberia).

31.   Drew JV, Tedrow JCF (1962) Arctic soil classification and patterned ground. *Arctic*, **15**, 109–116.

32.   Ellis CJ, Rochefort L, Gauthier G, Pienitz R (2008) Paleoecological evidence for transitions between contrasting landforms in a polygon-patterned high arctic wetland. *Arctic, Antarctic, and Alpine Research*, **40**, 624–637.

33.   Fiedler S, Wagner D, Kutzbach L, Pfeiffer E-M (2004) Element redistribution along hydraulic and redox gradients of low-centered polygons, Lena Delta, northern Siberia. *Soil Science Society of America Journal*, **68**, 1002–1011.

34.   Fortier D, Allard M, Shur Y (2007) Observation of rapid drainage system development by thermal erosion of ice wedges on Bylot Island, Canadian Arctic Archipelago. *Permafrost and Periglacial Processes*, **18**, 229–243.

35.   Frenzel P, Bosse U (1996) Methyl fluoride, an inhibitor of methane oxidation and methane production. *FEMS Microbiology Ecology*, **21**, 25–36.

36.   Galand PE, Yrjälä K, Conrad R (2010) Stable carbon isotope fractionation during methanogenesis in three boreal peatland ecosystems. *Biogeosciences*, **7**, 3893–3900.

37.   Godin E, Fortier D, Coulombe S (2014) Effects of thermo-erosion gullying on hydrologic flow networks, discharge and soil loss. *Environmental Research Letters*, **9**, 105010.

38.   Gupta V, Smemo KA, Yavitt JB, Fowle D, Branfireun B, Basiliko N (2013) Stable isotopes reveal widespread anaerobic methane oxidation across latitude and peatland type. *Environmental Science & Technology*, **47**, 8273–8279.

39.   Happell JD, Chanton JP, Showers WS (1994) The influence of methane oxidation on the stable isotopic composition of methane emitted from Florida swamp forests. *Geochimica et Cosmochimica Acta*, **58**, 4377–4388.

40.   Herndon EM, Mann BF, Chowdhury TR *et al*. (2015a) Pathways of anaerobic organic matter decomposition in tundra soils from Barrow, Alaska: biogeochemistry of Anoxic Arctic Tundra. *Journal of Geophysical Research: Biogeosciences*, **120**, 2345–2359.

41.   Herndon EM, Yang Z, Bargar J *et al*. (2015b) Geochemical drivers of organic matter decomposition in arctic tundra soils. *Biogeochemistry*, **126**, 397–414.

42.   Hershey AE, Northington RM, Whalen SC (2014) Substrate limitation of sediment methane flux, methane oxidation and use of stable isotopes for assessing methanogenesis pathways in a small arctic lake. *Biogeochemistry*, **117**, 325–336.

43.   Hines ME, Duddleston KN, Rooney-Varga JN ,Fields D, Chanton JP (2008) Uncoupling of acetate degradation from methane formation in Alaskan wetlands: Connections to vegetation distribution. *Global Biogeochemical Cycles*, **22**, GB2017.

44.   Hinkel KM, Nelson FE (2003) Spatial and temporal patterns of active layer thickness at Circumpolar Active Layer Monitoring (CALM) sites in northern Alaska, 1995–2000. *Journal of Geophysical Research: Atmospheres*, **108**, 8168.

45.   Hodgkins SB, Tfaily MM, McCalley CK *et al*. (2014) Changes in peat chemistry associated with permafrost thaw increase greenhouse gas production. *Proceedings of the National Academy of Sciences of the United States of America*, **111**, 5819–5824.

46.   Hornibrook ERC (2009) The stable carbon isotope composition of methane produced and emitted from northern peatlands. In: *Carbon Cycling in Northern Peatlands* (eds Baird AJ, Belyea LR, Comas X, Reeve AS, Slater LD), pp. 187–203. American Geophysical Union, Washington, DC.

47.   Hornibrook ER, Aravena R (2010) 6 Isotopes and methane cycling. In: *Environmental Isotopes in Biodegradation and Bioremediation* (eds Aelion CA, Hohener P, Hunkeler D, Aravena R). pp. 167–190. CRC Press, New York, NY.

48.   Hornibrook ERC, Longstaffe FJ, Fyfe WS (1997) Spatial distribution of microbial methane production pathways in temperate zone wetland soils: stable carbon and hydrogen isotope evidence. *Geochimica et Cosmochimica Acta*, **61**, 745–753.

49.   Hothorn T, Bretz F, Westfall P (2008) Simultaneous inference in general parametric models. *Biometrical Journal*, **50**, 346–363.

50.   Hubbard SS, Gangodagamage C, Dafflon B *et al*. (2013) Quantifying and relating land-surface and subsurface variability in permafrost environments using LiDAR and surface geophysical datasets. *Hydrogeology Journal*, **21**, 149–169.

51.   Huryn A, Hobbie J (2012) *Land of Extremes: A Natural History of the Arctic North Slope of Alaska*. University of Alaska Press, Fairbanks, AK..

52.   Johnston CE, Ewing SA, Harden JW *et al*. (2014) Effect of permafrost thaw on CO_2 and CH_4 exchange in a western Alaska peatland chronosequence. *Environmental Research Letters*, **9**, 085004.

53.   Jorgenson MT, Shur YL, Pullman ER (2006) Abrupt increase in permafrost degradation in Arctic Alaska. *Geophysical Research Letters*, **33**, L02503.

54.   Jorgenson MT, Harden J, Kanevskiy M *et al*. (2013) Reorganization of vegetation, hydrology and soil carbon after permafrost degradation across heterogeneous boreal landscapes. *Environmental Research Letters*, **8**, 035017.

55.   Kim Y (2015) Effect of thaw depth on fluxes of CO_2 and CH_4 in manipulated Arctic coastal tundra of Barrow, Alaska. *Science of the Total Environment*, **505**, 385–389.

56.   King GM (1992) Ecological aspects of methane oxidation, a key determinant of global methane dynamics. In: *Advances in Microbial Ecology* (ed. Marshall KC), pp. 431–468. Springer, Boston, MA.

57.   King SL, Quay PD, Lansdown JM (1989) The 13C/12C kinetic isotope effect for soil oxidation of methane at ambient atmospheric concentrations. *Journal of Geophysical Research: Atmospheres*, **94**, 18273–18277.

58.   Klapstein SJ, Turetsky MR, McGuire AD *et al*. (2014) Controls on methane released through ebullition in peatlands affected by permafrost degradation. *Journal of Geophysical Research: Biogeosciences*, **119**, 2013JG002441.

59.   Kotsyurbenko OR, Friedrich MW, Simankova MV, Nozhevnikova AN, Golyshin PN, Timmis KN, Conrad R (2007) Shift from acetoclastic to H2-dependent methanogenesis in a west Siberian peat bog at low pH values and isolation of an acidophilic Methanobacterium strain. *Applied and Environmental Microbiology*, **73**, 2344–2348.

60.   Koven CD, Ringeval B, Friedlingstein P *et al*. (2011) Permafrost carbon-climate feedbacks accelerate global warming. *Proceedings of the National Academy of Sciences of the United States of America*, **108**, 14769–14774.

61.   Kutzbach L, Wagner D, Pfeiffer E-M (2004) Effect of microrelief and vegetation on methane emission from wet polygonal tundra, Lena Delta, Northern Siberia. *Biogeochemistry*, **69**, 341–362.

62.   Kuznetsova A, Brockhoff PB, Christensen RHB (2014) lmerTest: Tests for random and fixed effects for linear mixed effect models (lmer objects of lme4 package). R package version 2.0-11.

63.   Lantz TC, Kokelj SV, Gergel SE, Henry GHR (2009) Relative impacts of disturbance and temperature: persistent changes in microenvironment and vegetation in retrogressive thaw slumps. *Global Change Biology*, **15**, 1664–1675.

64.   Lara MJ, McGuire AD, Euskirchen ES *et al*. (2014) Polygonal tundra geomorphological change in response to warming alters future CO_2 and CH_4 flux on the Barrow Peninsula. *Global Change Biology*, **21**, 1634–1651.

65.   Lawrence DM, Koven CD, Swenson SC, Riley WJ, Slater AG (2015) Permafrost thaw and resulting soil moisture changes regulate projected high-latitude CO_2 and CH_4 emissions. *Environmental Research Letters*, **10**, 094011.

66.   Le Mer J, Roger P (2001) Production, oxidation, emission and consumption of methane by soils: a review. *European Journal of Soil Biology*, **37**, 25–50.

67.   Liebner S, Ganzert L, Kiss A, Yang S, Wagner D, Svenning MM (2015) Shifts in methanogenic community composition and methane fluxes along the degradation of discontinuous permafrost. *Terrestrial Microbiology*, **6**, 356.

68.   Liljedahl AK, Hinzman LD, Schulla J (2012) Ice-wedge polygon type controls low-gradient watershed-scale hydrology. *Tenth International Conference on Permafrost, Salekhard, Russia*.

69.   Lipson DA, Zona D, Raab TK, Bozzolo F, Mauritz M, Oechel WC (2012) Water table height and microtopography control biogeochemical cycling in an Arctic coastal tundra Ecosystem. *Biogeosciences*, **9**, 577–591.

70.   Liptay K, Chanton J, Czepiel P, Mosher B (1998) Use of stable isotopes to determine methane oxidation in landfill cover soils. *Journal of Geophysical Research: Atmospheres*, **103**, 8243–8250.

71. MacKay JR (2000) Thermally induced movements in ice-wedge polygons, western arctic coast: a long-term study. *Géographie physique et Quaternaire*, **54**, 41.

72. Mancinelli RL (1995) The regulation of methane oxidation in soil. *Annual Reviews in Microbiology*, **49**, 581–605.

73. Mastepanov M, Sigsgaard C, Tagesson T, Ström L, Tamstorf MP, Lund M, Christensen TR (2013) Revisiting factors controlling methane emissions from high-Arctic tundra. *Biogeosciences*, **10**, 5139–5158.

74. McCalley CK, Woodcroft BJ, Hodgkins SB *et al.* (2014) Methane dynamics regulated by microbial community response to permafrost thaw. *Nature*, **514**, 478–481.

75. McGuire AD, Anderson LG, Christensen TR *et al.* (2009) Sensitivity of the carbon cycle in the Arctic to climate change. *Ecological Monographs*, **79**, 523–555.

76. McGuire AD, Christensen TR, Hayes D *et al.* (2012) An assessment of the carbon balance of Arctic tundra: comparisons among observations, process models, and atmospheric inversions. *Biogeosciences*, **9**, 3185–3204.

77. Miller KE, Lai C-T, Friedman ES, Angenent LT, Lipson DA (2015) Methane suppression by iron and humic acids in soils of the Arctic Coastal Plain. *Soil Biology and Biochemistry*, **83**, 176–183.

78. Minke M, Donner N, Karpov N, de Klerk P, Joosten H (2009) Patterns in vegetation composition, surface height and thaw depth in polygon mires in the Yakutian Arctic (NE Siberia): a microtopographical characterisation of the active layer. *Permafrost and Periglacial Processes*, **20**, 357–368.

79. Mondav R, Woodcroft BJ, Kim E-H *et al.* (2014) Discovery of a novel methanogen prevalent in thawing permafrost. *Nature Communications*, **5**, 3212.

80. Mook WG, Bommerson JC, Staverman WH (1974) Carbon isotope fractionation between dissolved bicarbonate and gaseous carbon dioxide. *Earth and Planetary Science Letters*, **22**, 169–176.

81. Natali SM, Schuur EAG, Mauritz M *et al.* (2015) Permafrost thaw and soil moisture driving CO_2 and CH_4 release from upland tundra. *Journal of Geophysical Research: Biogeosciences*, **120**, 525–537.

82. Newman BD, Throckmorton HM, Graham DE *et al.* (2015) Microtopographic and depth controls on active layer chemistry in Arctic polygonal ground. *Geophysical Research Letters*, **42**, 1808–1817.

83. Olefeldt D, Turetsky MR, Crill PM, McGuire AD (2013) Environmental and physical controls on northern terrestrial methane emissions across permafrost zones. *Global Change Biology*, **19**, 589–603.

84. Oremland RS, Taylor BF (1978) Sulfate reduction and methanogenesis in marine sediments. *Geochimica et Cosmochimica Acta*, **42**, 209–214.

85. Ping CL, Bockheim JG, Kimble JM, Michaelson GJ, Walker DA (1998) Characteristics of cryogenic soils along a latitudinal transect in Arctic Alaska. *Journal of Geophysical Research: Atmospheres (1984–2012)*, **103**, 28917–28928.

86. Ping CL, Jastrow JD, Jorgenson MT, Michaelson GJ, Shur YL (2015) Permafrost soils and carbon cycling. *SOIL*, **1**, 147–171.

87. Popp TJ, Chanton JP, Whiting GJ, Grant N (1999) Methane stable isotope distribution at a Carex dominated fen in north central Alberta. *Global Biogeochemical Cycles*, **13**, 1063–1077.

88. Rhew RC, Teh YA, Abel T (2007) Methyl halide and methane fluxes in the northern Alaskan coastal tundra. *Journal of Geophysical Research*, **112**, G02009.

89. Riordan B, Verbyla D, McGuire AD (2006) Shrinking ponds in subarctic Alaska based on 1950–2002 remotely sensed images. *Journal of Geophysical Research: Biogeosciences*, **111**, G04002.

90. Sachs T, Giebels M, Boike J, Kutzbach L (2010) Environmental controls on CH_4 emission from polygonal tundra on the microsite scale in the Lena river delta, Siberia: CONTROLS ON TUNDRA CH_4FLUX AND SCALING. *Global Change Biology*, **16**, 3096–3110.

91. Sannel ABK, Kuhry P (2011) Warming-induced destabilization of peat plateau/thermokarst lake complexes. *Journal of Geophysical Research: Biogeosciences*, **116**, G03035.

92. Schimel JP (1995) Plant transport and methane production as controls on methane flux from arctic wet meadow tundra. *Biogeochemistry*, **28**, 183–200.

93. Schuur EAG, Crummer KG, Vogel JG, Mack MC (2007) Plant species composition and productivity following permafrost thaw and thermokarst in Alaskan tundra. *Ecosystems*, **10**, 280–292.

94. Schuur EAG, Abbott BW, Bowden WB *et al*. (2013) Expert assessment of vulnerability of permafrost carbon to climate change. *Climatic Change*, **119**, 359–374.

95. Schuur EAG, McGuire AD, Schädel C *et al*. (2015) Climate change and the permafrost carbon feedback. *Nature*, **520**, 171–179.

96. Smith LC (2005) Disappearing Arctic lakes. *Science*, **308**, 1429.

97. Ström L, Ekberg A, Mastepanov M, Røjle Christensen T (2003) The effect of vascular plants on carbon turnover and methane emissions from a tundra wetland. *Global Change Biology*, **9**, 1185–1192.

98. Sturtevant CS, Oechel WC, Zona D, Kim Y, Emerson CE (2012) Soil moisture control over autumn season methane flux, Arctic Coastal Plain of Alaska. *Biogeosciences*, **9**, 1423–1440.

99. Tagesson T, Mölder M, Mastepanov M *et al*. (2012) Land-atmosphere exchange of methane from soil thawing to soil freezing in a high-Arctic wet tundra ecosystem. *Global Change Biology*, **18**, 1928–1940.

100. Torn MS, Chapin FS III (1993) Environmental and biotic controls over methane flux from Arctic tundra. *Chemosphere*, **26**, 357–368.

101. Torn MS, Davis S, Bird JA, Shaw MR, Conrad ME (2003) Automated analysis of 13C/12C ratios in $CO_2$and dissolved inorganic carbon for ecological and environmental applications. *Rapid Communications in Mass Spectrometry*, **17**, 2675–2682.

102. Tyler SC, Bilek RS, Sass RL, Fisher FM (1997) Methane oxidation and pathways of production in a Texas paddy field deduced from measurements of flux, δl3C, and δD of CH_4. *Global Biogeochemical Cycles*, **11**, 323–348.

103. Ulrich M, Grosse G, Strauss J, Schirrmeister L (2014) Quantifying wedge-ice volumes in Yedoma and thermokarst basin deposits. *Permafrost and Periglacial Processes*, **25**, 151–161.

104. Villarreal S, Hollister RD, Johnson DR, Lara MJ, Webber PJ, Tweedie CE (2012) Tundra vegetation change near Barrow, Alaska (1972–2010). *Environmental Research Letters*, **7**, 015508.

105. Von Fischer JC, Hedin LO (2007) Controls on soil methane fluxes: tests of biophysical mechanisms using stable isotope tracers. *Global Biogeochemical Cycles*, **21**, GB2007.

106. Von Fischer JC, Rhew RC, Ames GM, Fosdick BK, von Fischer PE (2010) Vegetation height and other controls of spatial variability in methane emissions from the Arctic coastal tundra at Barrow, Alaska. *Journal of Geophysical Research*, **115**, G00103.

107. Wagner D, Kobabe S, Pfeiffer E-M, Hubberten H-W (2003) Microbial controls on methane fluxes from a polygonal tundra of the Lena Delta, Siberia. *Permafrost and Periglacial Processes*, **14**, 173–185.

108. Wainwright HM, Dafflon B, Smith LJ *et al.* (2015) Identifying multiscale zonation and assessing the relative importance of polygon geomorphology on carbon fluxes in an Arctic Tundra Ecosystem. *Journal of Geophysical Research: Biogeosciences*, **120**, 788–808.

109. Walter KM, Edwards ME, Grosse G, Zimov SA, Chapin FS (2007) Thermokarst lakes as a source of atmospheric CH_4 during the last deglaciation. *Science*, **318**, 633–636.

110. Whalen SC, Reeburgh WS (1992) Interannual variations in tundra methane emission: a 4-year time series at fixed sites. *Global Biogeochemical Cycles*, **6**, 139–159.

111. Whiticar MJ (1999) Carbon and hydrogen isotope systematics of bacterial formation and oxidation of methane. *Chemical Geology*, **161**, 291–314.

112. Whiticar MJ, Faber E, Schoell M (1986) Biogenic methane formation in marine and freshwater environments: CO_2 reduction *vs.* acetate fermentation—Isotope evidence. *Geochimica et Cosmochimica Acta*, **50**, 693–709.

113. Wickland KP, Striegl RG, Neff JC, Sachs T (2006) Effects of permafrost melting on CO_2 and CH_4 exchange of a poorly drained black spruce lowland. *Journal of Geophysical Research: Biogeosciences*, **111**, G02011.

114. Xu L, Furtaw MD, Madsen RA, Garcia RL, Anderson DJ, McDermitt DK (2006) On maintaining pressure equilibrium between a soil CO_2 flux chamber and the ambient air. *Journal of Geophysical Research*, **111**, D08S10.

115. Ye R, Jin Q, Bohannan B, Keller JK, McAllister SA, Bridgham SD (2012) pH controls over anaerobic carbon mineralization, the efficiency of methane production, and methanogenic pathways in peatlands across an ombrotrophic–minerotrophic gradient. *Soil Biology and Biochemistry*, **54**, 36–47.

116. Yoshikawa K, Hinzman LD (2003) Shrinking thermokarst ponds and groundwater dynamics in discontinuous permafrost near council, Alaska. *Permafrost and Periglacial Processes*, **14**, 151–160.

117. Zona D, Lipson DA, Zulueta RC, Oberbauer SF, Oechel WC (2011) Microtopographic controls on ecosystem functioning in the Arctic Coastal Plain. *Journal of Geophysical Research*, **116**, G00108.